

MI-BMI_{net}: An Efficient Convolutional Neural Network for Motor Imagery Brain–Machine Interfaces with EEG Channel Selection

Xiaying Wang, *Student Member, IEEE*, Michael Hersche, *Student Member, IEEE*, Michele Magno, *Senior Member, IEEE*, Luca Benini, *Fellow, IEEE*

Abstract—A brain–machine interface (BMI) based on motor imagery (MI) enables the control of devices using brain signals while the subject imagines performing a movement. It plays an important role in prosthesis control and motor rehabilitation and is a crucial element towards the future Internet of Minds (IoM). To improve user comfort, preserve data privacy, and reduce the system’s latency, a new trend in wearable BMIs is to embed algorithms on low-power microcontroller units (MCUs) to process the electroencephalographic (EEG) data in real-time close to the sensors into the wearable device. However, most of the classification models present in the literature are too resource-demanding, making them unfit for low-power MCUs. This paper proposes an efficient convolutional neural network (CNN) for EEG-based MI classification that achieves comparable accuracy while being orders of magnitude less resource-demanding and significantly more energy-efficient than state-of-the-art (SoA) models for a long-lifetime battery operation. We propose an automatic channel selection method based on spatial filters and quantize both weights and activations to 8-bit precision to further reduce the model complexity with negligible accuracy loss. Finally, we efficiently implement and evaluate the proposed models on a parallel ultra-low power (PULP) MCU. The most energy-efficient solution consumes only 50.10 μ J with an inference runtime of 5.53 ms and an accuracy of 82.51% while using 6.4 \times fewer EEG channels, becoming the new SoA for embedded MI-BMI and defining a new Pareto frontier in the three-way trade-off among accuracy, resource cost, and power usage.

Index Terms—brain-machine interfaces, internet of minds, convolutional neural networks, feature extraction, embedded systems, edge computing

I. INTRODUCTION

A brain–machine interface (BMI) aims to translate brain activities into actionable information to control external devices, such as a wheelchair [1] or a prosthesis [2]. It is also used to assist rehabilitative processes [3], [4]. Besides clinical relevance for patients to regain lost abilities, recent developments have pushed the field of BMI towards everyday life tasks in consumer products [5], [6], for example, to control

robots [7], [8] or drones [9], yielding improved user experience also for healthy subjects [10]. Among the current BMI paradigms, motor-imagery (MI) is of great interest because it does not strictly depend on external stimuli; hence it can be independently and asynchronously self-paced [11]. The MI-BMI decodes the user’s intention by analyzing the brain activities while the subject thinks of a movement without actually performing it [12]. It enables the control of machines, such as ground vehicles [13], by merely using our minds, empowering the so-called future Internet of Minds (IoM) [14].

The key considerations for a successful wearable BMI are accuracy, user comfort, privacy preservation, low latency, and long battery lifetime [14]. Electroencephalogram (EEG)-based BMIs are the most commonly used non-invasive technique for acquiring brain signals by virtue of their relatively inexpensive nature and portability. The advent of wearable EEG devices with wireless data transmission has significantly improved user comfort [15]. However, they suffer from potential privacy concerns and a short battery lifetime because the acquired data is transmitted from the sensor node to a remote host such as tablets or computers for further processing. Recent achievements in low-power processing platforms and miniaturization enable the processing of sensor data directly at the edge. By embedding algorithms at the sensor node, the data is analyzed locally, preserving privacy, reducing the energy consumption for data transmission, and minimizing the system’s latency [16]. The decoded information can be directly sent to the controlled devices without any intermediate apparatus between our brains and the machines [14], [17], [18].

To achieve this goal, a smart wearable BMI has to satisfy the three-way trade-off among a) algorithmic performance: the embedded algorithm has to be able to accurately complete the targeted task; b) computational and storage parsimony: the complexity of the deployed algorithm has to meet the resource constraints of the edge platform in terms of memory footprint and runtime for a real-time application scenario; c) power: the power consumption must be low to guarantee a long-term continuous operation with long battery lifetime [16]. The low signal-to-noise ratio of the EEG data and the inter-session and inter-subject variability pose enormous challenges to obtaining high classification accuracy. Several machine learning (ML) and deep learning (DL) models have been proposed in the literature, achieving remarkable algorithmic performance [19], [20], [21]. However, the majority of them target only accuracy

Manuscript received November 07, 2019; revised January 16, 2020; accepted February 10, 2020.

X. Wang, M. Hersche, and L. Benini are with the Integrated Systems Laboratory, ETH Zürich, Switzerland (e-mail: xiaywang@iis.ee.ethz.ch). M. Magno is with the Center for Project-Based Learning D-ITET, ETH Zürich, Switzerland. M. Hersche is also with Cloud and AI Systems Research, IBM Research, Zürich, Switzerland. L. Benini is also with the Department of Electrical, Electronic and Information Engineering, University of Bologna, Italy.

This project was supported by the Swiss Data Science Center PhD Fellowship under grant ID P18-04.

as a key metric while ignoring the resources required by the model, making them unfit for low-power microcontroller units (MCUs). The Mr. Wolf processor [22] from the parallel ultra-low power (PULP) platform, a leading-edge example of high-performance and low-power MCU, has less than 600kB of on-chip fast memory and can deliver up to 16.4 Giga operations per second (GOPS) of computational capability while consuming less than 10mW [17]. It is specifically designed for edge processing, but even the EEGNet [23], which is well-known for its compact model size, is out of reach for embedding on this device by requiring more than 1 MB of memory to store intermediate results during inference computation [24]. Therefore, smaller models which demand fewer resources but at the same time maintain comparable accuracy are desirable [25].

Feature selection is an effective technique to reduce the number of features, yielding a smaller memory footprint and lower computational complexity. Especially for EEG applications, decreasing the number of EEG channels brings the benefit of not only a reduced number of computations but also lower power consumption since fewer analog front-end circuits are necessary for the data acquisition. However, a reduced number of channels makes the task even more difficult, often causing accuracy degradation [24]. Hence, sophisticated methods for channel selection are necessary to extract relevant features for the task while maintaining accurate performance [26], [27], [28]. Another commonly used technique to reduce the resource requirements is quantization, e.g., using 8 bits to represent numbers instead of 32 bits [29], [30]. This yields a significant reduction in memory usage and allows the use of efficient hardware units. However, reduced numerical precision can lead to accuracy loss; hence, sophisticated algorithms are necessary to guarantee comparable performance [30], [18].

In this paper, we propose an end-to-end workflow for the realization of a smart, energy-efficient, and wearable BMI for MI classification, starting from the design of a resource-friendly yet accurate convolutional neural network (CNN), moving to further model reduction by selecting relevant EEG channels and by quantizing to lower bit precision, and finally focusing on hardware deployment on a low-power MCU for an embedded smart wearable BMI with low latency and extended battery lifetime, paving the way to the future IoM. The main contributions are as follows:

- An efficient CNN for MI-BMI classification that meets the tight resource constraints of a low-power MCU while being as accurate as the resource-demanding state-of-the-art (SoA) algorithms. We apply our model on two publicly available MI datasets, namely the BCI Competition IV-2a dataset and Physionet Motor Movement/Imagery (MM/MI) dataset, to evaluate its performance in both inter-session and inter-subject challenges and achieve respectively 76.03%, 65.62% accuracy on the 4-class task and 86.32%, 82.79% on the 2-class task.
- A channel selection and reduction method that automatically selects the most relevant EEG channels based on the spatial filters of the proposed CNN to further reduce the model complexity and the memory footprint while maintaining similar classification accuracy (82.79% vs.

82.51% for the 2-class task of the MM/MI dataset) or even improving the accuracy by up to 1.33% in the case of the subject-specific models of the IV-2a dataset.

- We quantize both weights and activations of the proposed CNN to 8-bit representations with negligible effect on the classification accuracy (less than 0.4% accuracy drop) to further reduce the model size and to exploit the hardware architecture of the selected MCU for an optimized embedded implementation. We efficiently deploy the quantized model on PULP Mr. Wolf [22] and experimentally measure the power consumption and model execution runtime. Our best solution for the 2-class task of the MM/MI dataset consumes 9.06mW and takes only 5.53ms, yielding an energy usage of only 50 μ J per inference, using only 10 EEG channels instead of 64.

This work successfully satisfies the three-way trade-off among performance, cost, and power [16] by maximizing the algorithmic accuracy, minimizing the computational cost, and minimizing the power consumption for a real-time smart wearable MI-BMI for long-term usage.

II. RELATED WORKS

Traditional ML-based approaches in MI-BMI require manual extraction of features, based on which a classifier is trained to solve the underlying task. Common Spatial Patterns (CSP) is one of the most commonly used techniques in MI-BMI to extract the most discriminative spatial features between two classes of EEG signals [38]. Many variants and improvements have been proposed to increase the classification accuracy, such as Filter-Bank Common Spatial Patterns (FBCSP) by Ang et al. [39]. These approaches are improved by Das et al. [31] with FBCSP and Adaptive Boosting, resulting in a Cohen's kappa value of 0.646 on the 4-class BCI Competition IV-2a dataset in pair-wise configuration. Another class of effective feature extractors used in BMI is based on the Riemannian geometry [40]. The work in [32] compares the CSP and Riemannian methods using large multiscale temporal and spectral features. The results demonstrate that Multiscale Riemannian Classifier (MRC) achieves the best classification accuracy of 75.47% using multiple time windows with support vector machine (SVM) in pair-wise classification.

In another vein, DL methods enable the classification of BMI tasks without manual feature engineering. Inspired by FBCSP, Schirrmeyer et al. [19] propose the use of CNNs to automatically learn features from EEG signals and classify different imagined movements. The results demonstrate that the proposed deep and shallow ConvNets can reach up to 5.7% better accuracy (73.7%) than FBCSP (68%) without the need for handcrafted features. A similar CNN architecture based on shallow ConvNet is used by Dose et al. [37], achieving 80.38%, 69.82%, and 58.58% in 2-, 3-, and 4-class MI tasks on the Physionet MM/MI dataset [41]. More recent works [20], [21] have proposed similar but much bigger CNNs, respectively achieving 75.8% and 86.96% accuracy on the 4- and 2-class tasks of the IV-2a dataset. One major drawback of the DL approach is that the models tend to grow in size, yielding increased demand for computational

TABLE I: Related works. The accuracy [%] and the kappa value are reported with full-channel configuration before quantization if not otherwise stated. The estimated computational resources are calculated with full-channel setup on the 4-class task when available, otherwise on the 2-class task. The proposed solution and the best values of each column are highlighted in bold.

	Accuracy / Kappa Value			Tot. # params	Max. f. map size	Tot. # MACC	Channel reduction	Quanti- zation	Deploy- ment	Runtime, avg. power
	2-	3-	4-class							
BCI Comp. IV-2a dataset										
FBCSP [31]	-/-	-/-	-/0.65	-	-	-	None	None	None	-
MRC [32]	-/-	-/-	75.47/-	-	-	-	None	None	None	-
MSFBCNN [20]	-/-	-/-	75.80/-	155 k	5,775 k	202 M	None	None	None	-
FB+3D-CNN [21]	86.96/-	-/-	-/-	46 M	472.1 k	62.3 M	None	None	None	-
S. ConvNet [19]**	79.90/-	-/-	74.31/0.66	47.3 k	1,013 k	63.0 M	None	None	None	-
EEG-TCNet (fixed) [33]	-/-	-/-	77.35/0.70	4.27 k	396 k	6.8 M	None	None	None	-
E-CSP [26]†	83.61/-	-/-	-/-	-	-	-	Automatic	None	None	-
CSP+Riemannian [34]‡	-/-	-/-	77.82/0.71	-	-	-	Automatic	None	None	-
WOLACSP [35]	78.85/-	-/-	-/-	-	-	-	None	None	FPGA	430 ms, 700 mW
CSP+SVM [36]	80.55/-	-/-	67.21/-	-	-	-	None	20-bit	FPGA	11.66 ms, 83.90 mW
EEGNet [23], [18]	-/-	-/-	71.30/-	2.63 k	223 k	12.98 M	None	8-bit	MCU	28.67 ms, 11.75 mW
MI-BMInet (Proposed)	86.32/0.73	80.37/0.71	76.03/0.68	6.08 k	40.5 k	2.21 M	Automatic	8-bit	MCU	11.37 ms, 10.07 mW
87.65/0.75‡	81.52/0.72‡	77.18/0.70‡								10.57 ms, 9.7 mW†
Physionet MM/MI dataset										
S. ConvNet [37]	80.38/-	69.82/-	58.58/-	203 k	1,260 k	86.12 M	Manual	None	None	-
CNN [28]	83.26/-	-/-	-/-	235 k	122.88 k	33.61 M	Automatic	None	None	-
EEGNet [23], [24]	82.29/-	74.46/-	64.85/-	3.2 k	277.56 k	31.98 M	Manual	None	MCU	20.40 ms, 413.06 mW
MI-BMInet (Proposed)	82.79/-	74.92/-	65.62/-	4.23 k	38.40 k	1.51 M	Automatic	8-bit	MCU	6.21 ms, 9.97 mW
82.51/-	74.21/-	63.93/-								5.53 ms, 9.06 mW§

** Respectively reproduced in [21] and [33] for 2- and 4-class tasks. ‡ Mean accuracy with subject-specific number of selected channels.

† Subject 8 with 6 EEG channels for the 2-class task. || Respectively with 10, 20, and 18 selected channels. § 10 channels for the 2-class task.

and storage resources. Especially for very low-power MCUs in the sub-100-milliwatt power range, e.g., Mr. Wolf that has up to 512 kB on-chip memory and 16.4 GOPS of computational capability, even the shallow version of the ConvNet [19], [37] is out-of-reach by requiring an estimated 0.8 MB for storing the model parameters and 5.2 MB for intermediate feature maps during execution in 32-bit precision. Lawhern et al. [23] propose a much more compact CNN called EEGNet. By employing depthwise convolution, the number of model parameters is significantly reduced down to only a few tens of kB. A similarly small network called EEG-TCNet [33] is recently proposed improving the accuracy considerably. Nevertheless, the challenge remains for storing intermediate results during the model execution using only on-chip fast memory. Assuming the model execution with a layer-by-layer schedule, the two biggest consecutive feature maps dictate the amount of required memory. In the case of EEGNet, all the input EEG channels and the output of the first temporal convolution layer have to be stored in memory, adding up to almost 300k values [24], meaning more than 1 MB in 32-bit representation or around 300 kB in 8-bit precision. In this paper, we propose a more compact CNN with up to $7.2\times$ reduction in the memory usage for the feature maps compared to EEGNet, while being up to 4.73% more accurate on the IV-2a dataset, as reported in Table I.

Additionally, feature selection allows to reduce the number of features and to identify the most relevant ones, usually yielding improved performance and fewer computations. In EEG-based applications, it is beneficial to reduce the number of EEG channels directly. Using fewer electrodes means decreased power consumption for data acquisition and com-

putation, improved user comfort, and reduced setup time for the acquisition headset. Subject-specific channel selection has proven to be advantageous also for increasing classification accuracy [26], [34]. The authors in [34] combine CSP with Riemannian distances obtaining a classification accuracy of 77.82% and a kappa value of 0.7086 with an average of 15.2 selected channels over the nine subjects of the IV-2a dataset for the 4-class MI task. CNN-based channel reduction approaches are also found in the literature [37], [28]. Dose et al. [37] manually select subsets of EEG channels to compare with related works and demonstrate that their proposed architecture based on shallow ConvNet outperforms most of the other models. More recent work by Tokovarov et al. [28] applies an automatic channel selection method based on CNN feature maps obtaining 82.34% accuracy with only 14 instead of 64 channels on the 2-class MI task of the MM/MI dataset outperforming the manual selection of [37]. Given the many advantages of channel selection, we propose in this work an automated method based on the spatial filters of the proposed CNN. It can effectively reduce the number of channels by 84%, i.e., from 64 to 10, for the MM/MI dataset, with the advantage of $1.3\times$ fewer parameters, $3.1\times$ less memory footprint, and $1.4\times$ lower computational complexity while having a negligible accuracy drop of 0.28% for the 2-class inter-subject task. The inter-session accuracy of the subject-specific models for the IV-2a dataset is increased by up to 1.33%, with an average channel reduction of 60% for the 2-class task.

Embedded deployment of ML and DL models on low-power edge devices has been gaining increasing attention in the ML community, giving birth to notable projects such as

TensorFlow Lite [42] and TinyML [43]. Some initial efforts can also be found in BMI literature. However, most of the BMI algorithms, especially the ones for MI, are too resource-demanding for low-power MCUs. In contrast, edge devices with more resources are too power-hungry and might not meet the specifications for long-term usage. Belwafi et al. [35] propose a CSP-based approach with weighted overlap-add (WOLA) filters to extract subject-specific frequency bands and use linear discriminant analysis (LDA) to classify left and right MI tasks from the IV-2a dataset, obtaining 78.85% accuracy. The proposed method is subsequently implemented on a Stratix-IV field-programmable gate array (FPGA) board, taking 430 ms per inference and consuming 700 mW. Another embedded implementation can be found in [36]. The authors employ a CSP-based feature extractor, mutual information as feature selector, LDA to reduce features, and SVM for the final classification. The accuracy on the IV-2a dataset is 80.55% and 67.21% for 2- and 4-class tasks, respectively. The methods are implemented on a Virtex-6 FPGA consuming 83.90 mW and taking up to 11.66 ms.

Two other works have implemented DL-based approaches for MI-BMI on embedded devices [24], [18]. The authors in [24] deploy an EEGNet-based CNN on two MCUs featuring ARM Cortex-M4 and M7, yielding a power consumption of 42.44 mW and up to 413.06 mW, respectively. The input signals are downsampled, shortened in time, and 38 manually selected EEG channels are used to deploy the models within the constrained resources. The accuracy for the 4-class MI task drops negligibly from 65.07% to 64.76% on the Cortex-M7, which consumes one order of magnitude more power than the Cortex-M4 but has more resources. Whereas, the decrease in accuracy on the Cortex-M4 is more accentuated, i.e., -2.56%. The inference time is around 100 ms for the M4 and down to 20.40 ms on the M7 for the same model. A more energy-efficient implementation is proposed in [18]. The model is first quantized to 8-bit fixed-point representation with negligible loss in accuracy and implemented on Mr. Wolf, a RISC-V-based PULP platform with parallel processing units [22]. The average quantized accuracy over the nine subjects of the IV-2a dataset is 70.9% for the 4-class MI task. The energy consumption is only 337 μ J and the inference time is 28.67 ms. However, the proposed solution is designed explicitly for EEGNet, and it abandons the common layer-by-layer computation paradigm adopted by most deployment frameworks. Moreover, no channel reduction has been explored to further reduce the complexity and improve the energy-efficiency. Similarly to [18], we quantize our proposed CNN to 8 bits achieving 4.73% higher accuracy. We further reduce the number of EEG channels for a more energy-efficient implementation. Our solution achieves a lower energy consumption of 103 μ J and 50 μ J, respectively for IV-2a and MM/MI datasets, which is 3.3 \times and 6.7 \times less energy consumption than the previous most energy-efficient solutions [18], [24].

Table I summarizes the discussed related works. For a smart wearable MI-BMI device that guarantees the benefits of privacy preservation, low latency response, and long-term battery life, the golden triangle of accuracy performance, resource requirements, and power consumption has to be satisfied [16].

While maintaining accurate classification performance, efficient models that meet the resource constraints of low-power MCUs are desired. Specifically for EEG-based BMI applications, reducing EEG channels yields improved wearability and fewer computations, thus lower power consumption. Further techniques such as quantization to lower numerical precision leads to optimized and energy-efficient embedded deployments by exploiting the underlying Instruction Set Architecture (ISA) for an optimal hardware/software co-design. Our work integrates all these aspects and satisfies the three-way trade-off among performance, resource usage, and power for the next-generation smart wearable BMIs. The workflow proposed in this paper is as follows: first, the BMI challenges are identified and the relevant datasets are chosen; second, an accurate classification model is designed by taking into consideration the hardware constraints; third, feature selection is performed to reduce the number of EEG channels yielding more energy-efficient models; fourth, the model is quantized to further minimize the resource usage; finally, the quantized model is efficiently implemented on a low-power MCU. The following sections are organized accordingly.

III. DATASETS

EEG-based BMIs suffer from inter-session and inter-subject variability that poses considerable challenges to designing accurate models. Two SoA MI datasets are used in this work to tackle both, respectively the IV-2a from the famous BCI Competition [44], [45] and the newer and much larger Physionet EEG MM/MI [46], [41].

1) *BCI Competition IV-2a*: Four MI tasks are recorded from 9 subjects using 22 EEG channels, namely the imagined movements of the left hand (L), right hand (R), both feet (F), and tongue (T). The data is collected at 250 Hz sampling frequency and provided after a bandpass filter between 0.5 Hz and 100 Hz. Following the competition rules, the three additional electrooculography channels are not considered. Two sessions of recordings from two different days are available, each containing 288 trials. The first session is used as the training set, while the second is used for testing. The dataset provides notes for artifacts removal marked by an expert resulting in 9.41% of the trials being removed. Fig 1 shows the timing scheme of one trial, where the participants see a fixation cross for 2 s, then the cue appears, and they are asked to start imagining the cued movement after 1 s. The MI lasts 3 s followed by a break. In this work, we perform 2-, 3-, and 4-class classification using L/R, L/R/F, and L/R/F/T MI tasks, respectively, and consider a time window of 3 s starting from the appearance of the cue.

2) *Physionet EEG MM/MI*: The dataset contains EEG recordings of 109 subjects while performing motor movement and MI tasks. It is recorded at a sampling rate of 160 Hz using 64 electrodes according to the international 10-10 system (omitting the channels Nz, F9, F10, FT9, FT10, A1, A2, TP9, TP10, P9, and P10). In this work, only MI data is evaluated. Due to differences in the number of trials, four subjects (88, 92, 100, 104) are discarded, resulting in 105 subjects being effectively considered. Every subject performed a total of six

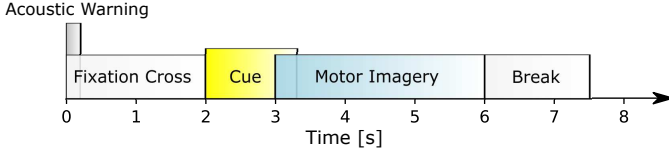


Fig. 1: Timing scheme of BCI Competition IV-2a [44].

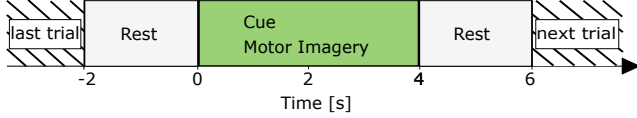


Fig. 2: Trial scheme of Physionet EEG MM/MI Dataset [46]

MI runs: three runs of the left fist (L) against the right fist (R) and three runs of both fists (B) against both feet (F). Each run consists of 14 trials following the time scheme shown in Fig. 2. The subject performs one of the four MI tasks, when the MI cue is shown. In total, we have 21 trials per class per subject. Additionally, two baseline runs with resting data are provided while the subjects did not receive any visual cue and had their eyes open and closed. We extract windows of 3 s from the eyes open baseline run to obtain trials with resting EEG data (0). As in [37], we perform 2-, 3-, and 4-class MI classification using L/R, L/R/0, and L/R/0/F MI tasks, respectively, and consider a time window of 3 s starting from the appearance of the cue.

IV. NETWORK ARCHITECTURE

This section describes the first main contribution of the paper: we propose *MI-BMInet*, a light-weighted yet accurate CNN for EEG-based MI-BMIs that is suitable for low-power MCUs on smart edge wearable devices.

A. edgeEEGNet

Fig. 3 depicts the architecture of the proposed model. The input array is arranged such that each row represents the EEG signals from the electrodes, and each column is the sample at every time point. The dimension is $N_{ch} \times N_s$, with N_{ch} being the number of EEG channels and N_s the number of samples. The input is passed to a first depthwise convolutional layer with N_k one-dimensional kernels of size $N_{ch} \times 1$ to find spatial correlations among the EEG channels, followed by a batch normalization layer. This spatial convolution outputs N_k feature maps of dimension $1 \times N_s$. These are subsequently filtered using another layer of depthwise convolution with N_k kernels of dimension $1 \times N_f$ applied along the temporal dimension to learn temporal information. Afterwards, a separable convolution, i.e., a depthwise convolution followed by a pointwise convolution, is applied to further extract spatio-temporal features using N_k filters of size 1×16 . Rectified Linear Unit (ReLU) is chosen as activation since it is the most hardware-friendly non-linear activation function. Additionally, average pooling layers with a kernel size of 8×1 are applied in the time domain to reduce the dimensions of the feature maps. Finally, a fully connected layer gives the classification output with N_{cl} classes.

B. Resource requirements

For deploying a model on resource-constrained low-power edge devices, it is necessary to assess the model's memory footprint and computational complexity.

MI-BMInet contains two depthwise and one separable convolutions, each with N_k filters. The number of parameters in a depthwise convolutional layer can be calculated as $N_k \cdot (k_H \cdot k_W)$, with k_H and k_W being respectively the height and width of the kernels, reported in brackets in Fig. 3. While in the separable convolutional layer there are $N_k \cdot (1 \cdot 16) + N_k \cdot N_k$ parameters. Additionally, each batch normalization layer has $4 \cdot f$ parameters, with f being the number of feature maps, which corresponds to the number of filters N_k in the case of depthwise convolutions. Finally, a fully connected layer with n_{in} input nodes and n_{out} output nodes presents $(n_{in} + 1) \cdot n_{out}$ parameters. Besides the weights of the network, also the input and the output feature maps need to be stored during the computation of a layer; hence we also compute the feature maps' size as the number of filters multiplied by the output shape. As an example, the size of the input and the output feature maps of the first convolutional layer is $N_{ch} \cdot N_s + N_k \cdot N_s$, which has to be stored contemporaneously in the memory during the computation time.

We further estimate the complexity of the model as the sum of the number of multiply-and-accumulate (MACC) operations in the convolutional and fully connected layers. The number of operations in each depthwise convolutional layer is $(k_H \cdot k_W) \cdot (H_{out} \cdot W_{out}) \cdot N_k$, with H_{out} and W_{out} being respectively the height and the width of the output feature maps. While for the separable convolution we estimate $(H_{out} \cdot W_{out}) \cdot ((1 \cdot 16) + N_k)$ MACC operations. Finally, the fully connected layer requires $n_{in} \cdot n_{out}$ operations.

V. EEG CHANNEL SELECTION

This section presents the second main contribution of the paper. Selecting the most relevant EEG channels and reducing the number of EEG electrodes yields not only more user comfort and less obtrusiveness but also lower power consumption and longer lifetime for a wearable device: fewer circuits, e.g., analog-to-digital converters (ADCs), are used in the acquisition, at the same time the memory footprint and the computational complexity are reduced for the data processing. Hence, before deploying the trained models on the MCUs for edge inference, we first reduce the number of EEG channels by proposing a novel, automatic channel selection method based on the weights of the spatial convolution. For comparison, we additionally implement two manual channel selection methods: one based on the whole scalp as in [24], while the other one targets the specific brain region such that the EEG electrodes can be embedded into smart wearable headphones, e.g., Versus headset [47] or Melomind [48].

A. Automatic Channel Selection based on Spatial Filters

Given a pretrained model on all N_{ch} EEG channels and W_S the weights of the first spatial convolutional layer with

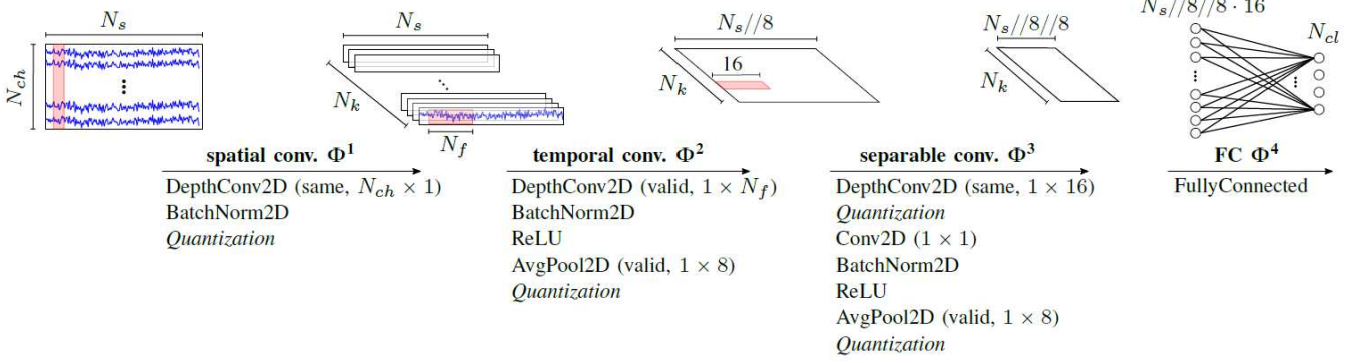


Fig. 3: Architecture of *MI-BMInet*. N_s is the number of input samples in the time domain, N_{ch} the number of EEG channels, N_{cl} the number of classes, N_f the filter size of the temporal filter, and N_k is the number of filters. The padding strategy and the kernel size are reported in brackets. The addition of the quantization layers is highlighted in *italic*.

dimension $N_{ch} \times N_k$, we compute the ℓ_2 -norm for each EEG channel $i_{ch} = 1, 2, \dots, N_{ch}$ as

$$\|w_S\|_2(i_{ch}) = \sqrt{\sum_{n=1}^{N_k} |w_S(i_{ch}, n)|^2}, \quad (1)$$

which gives the vector's magnitude of the weights corresponding to each EEG channel. We subsequently select \bar{N}_{ch} channels with the biggest $\|w_S\|_2$ amplitudes, with \bar{N}_{ch} being the desired number of EEG electrodes. Algorithm 1 shows the pseudo-code of the proposed method.

TABLE II: EEG electrodes configurations using headset-based channel selection over sensorimotor and neighboring areas. The regions correspond to the brain areas with color-shaded background illustrated in Fig. 4, as well as the electrodes, while N_{ch} is the number of selected channels.

Region	N_{ch}	Electrodes
Central (C)	2	C3, C4
	3	C3, CZ, C4
	5	C5, C3, CZ, C4, C6
	7	C5, C3, C1, CZ, C2, C4, C6
	9	T7, C5, C3, C1, CZ, C2, C4, C6, T8
11	T9, T7, C5, C3, C1, CZ, C2, C4, C6, T8, T10	
C+Frontal	4	C3, C4, FC3, FC4
	6	C3, CZ, C4, FC3, FCZ, FC4
	10	C5, C3, CZ, C4, C6, FC5, FC3, FCZ, FC4, FC6
	14	C5, C3, C1, CZ, C2, C4, C6, FC5, FC3, FC1, FCZ, FC2, FC4, FC6
	18	T7, C5, C3, C1, CZ, C2, C4, C6, T8, FT7, FC5, FC3, FC1, FCZ, FC2, FC4, FC6, FT8
20	T9, T7, C5, C3, C1, CZ, C2, C4, C6, T8, T10, FT7, FC5, FC3, FC1, FCZ, FC2, FC4, FC6, FT8	
C+Parietal	4	C3, C4, CP3, CP4
	6	C3, CZ, C4, CP3, CPZ, CP4
	10	C5, C3, CZ, C4, C6, CP5, CP3, CPZ, CP4, CP6
	14	C5, C3, C1, CZ, C2, C4, C6, CP5, CP3, CP1, CPZ, CP2, CP4, CP6
	18	T7, C5, C3, C1, CZ, C2, C4, C6, T8, TP7, TP5, CP3, CP1, CPZ, CP2, CP4, CP6, TP8
20	T9, T7, C5, C3, C1, CZ, C2, C4, C6, T8, T10, TP7, CP5, CP3, CP1, CPZ, CP2, CP4, CP6, TP8	

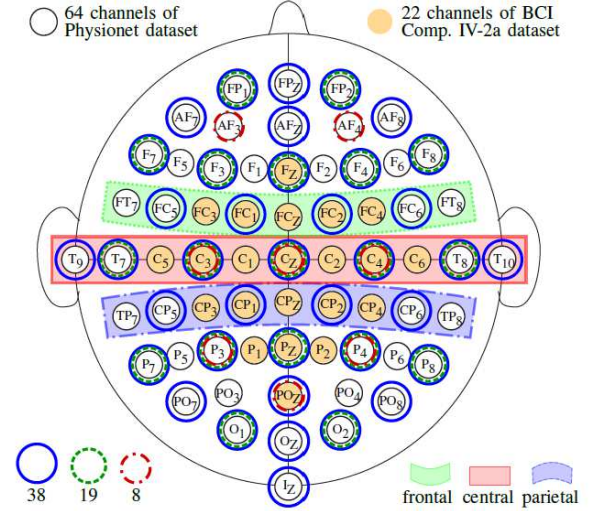


Fig. 4: Electrode configurations for manual channel selections.

B. Manual Channel Selections

Fig. 4 shows the positions of the 64 electrodes for the MM/MI dataset and the 22 channels filled with yellow used

Algorithm 1: Pseudo-code for automatic EEG channel selection based on spatial filters of the proposed CNN.

Data: Pretrained model on all N_{ch} channels.

Result: Indexes of \bar{N}_{ch} selected channels.

begin

Load the pretrained model;
 Extract W_S , the weights of the spatial convolution;
for each EEG channel i_{ch} **from** 0 **to** $N_{ch} - 1$ **do**
 Calculate the ℓ_2 norm

$$\|w_S\|_2(i_{ch}) = \sqrt{\sum_{n=1}^{N_k} |w_S(i_{ch}, n)|^2}$$

Find the indices that sort $\|w_S\|_2(i_{ch})$ in descending order;

Take the first \bar{N}_{ch} indices;

end

in the IV-2a dataset. To directly compare with [24] on the MM/MI dataset, we select three configurations that are evenly distributed over the entire scalp:

- 19 electrodes based on the international 10-20 system (excluding A1 and A2), encircled with green dashed lines;
- 38 electrodes are selected by adding intermediate positions, encircled with solid blue lines;
- 8 electrodes based on Bitbrain headset, encircled with dash-dotted red lines.

The distributed configurations are not evaluated on IV-2a because of the reduced number of available electrodes (22) in this dataset.

Furthermore, we manually select the EEG channels covering the sensorimotor cortex, where most of the brain’s activations during motor-movement (MM) and MI are identified, especially around C3 and C4 [49], [12]. This region is also physically covered by the audio headphones that are commonly accepted and worn nowadays for long periods of time by the users. This means we can embed the EEG electrodes on a wearable device already widely used in daily life. This setup is much less obtrusive and aesthetically more acceptable than traditional EEG caps. Hence, we select subsets of electrodes from the central line covering the C3 and C4 electrodes as highlighted in Fig. 4 with the red-shaded background. In addition, we separately and incrementally include subsets of adjacent electrodes towards the front and the back of the head, respectively shaded with green and blue background color in Fig. 4. Table II reports all the configurations with the selected subsets of channels over the sensorimotor cortex for the MM/MI dataset. The same is done for the IV-2a dataset with the available electrodes.

C. Training and Evaluation Protocols

We first train and validate our models using all channels to set the baseline. Afterwards, we reduce the input data by selecting subsets of channels. This allows us to train new models from scratch with a reduced number of parameters and smaller feature map sizes for the subsequent deployment on resource-constrained MCUs. For both baseline and reduced models, we use the following protocols for the two datasets using Keras with TensorFlow (version 1.11) backend:

1) *BCI Competition IV-2a*: As in [18], [32], we perform subject-specific validation using the first session for training and the second for testing to account for inter-session variability, as stated in the competition rules. The model is trained with Adam optimizer for 500 epochs with a batch size of 32, a fixed learning rate of 0.001, and $1e-7$ as the default epsilon value for numerical stability. The cross-entropy loss is used. We repeat the experiments 25 times and report the average accuracy to consider the training variability.

2) *Physionet EEG MM/MI*: Validation is performed using 5-fold cross-validation (CV) across the subjects, as in [24], by considering the inter-subject variability. The model is trained with Adam optimizer for 100 epochs with a batch size of 16. A fixed learning rate scheduler reaches the best performance; more precisely, the learning rate is set to 0.01, 0.001, and 0.0001 at epochs 0, 40, and 80, respectively. Cross-entropy

loss is used. We repeat the 5-fold CV experiments 5 times and report the average results.

VI. EMBEDDED IMPLEMENTATION

This section summarizes the third main contribution of the paper. To optimally deploy *MI-BMInet* on low-power MCUs, we first quantize the models to 8-bit representations using quantization-aware training to further reduce the memory footprint and to exploit the hardware extensions. Subsequently, we deploy the quantized networks on the selected MCU and measure the runtime and the power consumption.

A. Quantization

We quantize both weights and activations of *MI-BMInet*, including the input signals, from 32-bit floating-point representation to 8-bit fixed-point values with quantization-aware training. The addition of the quantization layers is shown in Fig. 3. The quantization procedure is as follows:

- The network is trained in full precision until epoch t_a ;
- at epoch t_a , the quantization of the activations starts using the straight-through estimator (STE) [50]. The network is readjusted on the quantized activations until epoch t_w ;
- from epoch t_w until epoch t_{end} , the weights are increasingly quantized using Random Partition Relaxation (RPR) [30] at a step size of 10.

For the IV-2a dataset, the epochs are chosen to be $t_a=450$, $t_w=550$, and $t_{end}=650$, as in [18]. We use the cross-entropy loss and the Adam optimizer with a fixed learning rate of 0.001 and $\text{eps}=1e-7$. While for the MM/MI dataset we tune the quantization and obtain the best results with $t_a=60$, $t_w=160$, and $t_{end}=260$. For the 3- and 4-class tasks, a fixed learning rate of 0.001 and $\text{eps}=1e-9$ are used. Whereas for the 2-class task, the same learning rate scheduler as in Sec. V-C is used with $\text{eps}=1e-9$. The training and the validation procedures are implemented in PyTorch based on the Quantlab framework [29].

B. Network Deployment and Measurements

We implement the 8-bit quantized networks on RISC-V-based PULP Mr. Wolf [22]. Its compute cluster is equipped with 8 parallel cores with custom ISA extensions and an L1 Tightly Coupled Data Memory (TCDM) of 64 kB, while an additional 512 kB of on-chip L2 memory is present in the System-on-Chip (SoC) domain. A Direct Memory Access (DMA) unit can handle the data transfer between the L1 and the L2 autonomously.

As in [18], we merge the conversion factor of the quantization with the bias and the scaling factor of the batch normalization layers and reorder the batch normalization, the ReLU, and the pooling layers to reduce the number of divisions, since they are expensive operations requiring many computational cycles and introduce rounding errors. Moreover, we exploit the Single Instruction, Multiple Data (SIMD) operations and the 8 parallel cores to speed up the computation and use the optimized 1-D cross-correlation functions from the PULP-DSP library [51] by exporting the network weights in the reversed order. Different from [18], we reimplement the data handling

and the computation of layers Φ^1 and Φ^2 to efficiently exploit the data locality and use the SIMD operations.

We measure the power consumption and the inference runtime of the deployed models using the Keysight N6705B power analyzer.

VII. EXPERIMENTAL RESULTS

In this section, we present and discuss the performance of the proposed energy-efficient CNN in terms of classification accuracy, computational complexity, and memory footprint. Moreover, the outcome of the novel channel selection method is presented and compared to manual baselines and related works. Finally, the quantization results are reported, followed by experimental measurements of the power consumption and the runtime of the deployed models on the selected edge platform.

The classification accuracy is reported as an average over the repetitions and across the 9 subjects for the IV-2a and the 5 CV folds for the MM/MI dataset. The Cohen’s kappa score is also calculated for the IV-2a as it is often done with this dataset.

A. Network architecture

Based on the performance achieved with hyperparameters tuning, we choose the filter size N_f to be 64 and 128, the number of filters N_k to be 32 and 16 for the IV-2a and the MM/MI dataset, respectively. As reported in Table IIIa, our model requires around 6.1k and 4.2k parameters in full-channel configuration. Adopting the most common layer-by-layer computation, we need to store the input and the output feature maps of a layer during inference execution. Hence, the two biggest consecutive feature maps dictate the required memory footprint. In our case, the execution of *MI-BMInet* requires up to 40.5k and 38.4k features to be stored, respectively for the IV-2a and the MM/MI dataset. The accuracy in

32-bit floating-point representation using all EEG channels is reported in Table IIIb.

Compared to the related works in Table I, *MI-BMInet* requires up to two orders of magnitude less memory for storing the model parameters. EEGNet [18], [24] is the only one that requires less storage for the model parameters; however, the memory footprint for the feature maps is $5.5\times$ and $7.2\times$ more than our proposed models, respectively, for IV-2a and MM/MI datasets. The significant memory demand during inference runtime has caused the deployment of EEGNet to be trickier and more time-consuming [18] while also causing accuracy degradation [24]. The proposed solution effectively solves the issue with the memory footprint while achieving up to 4.73% better accuracy in the full-channel configuration on the IV-2a dataset. When comparing the computational complexity, *MI-BMInet* requires the least number of MACC operations, i.e., down to 2.21 million for the IV-2a dataset and 1.51 million for the MM/MI dataset. Compared to the most compute-intensive related works [20], [37], our models require $91\times$ and $57\times$ less computation, while being 0.23% and 7.04% more accurate, respectively on IV-2a and MM/MI datasets.

Despite the limited resource requirements, the accuracy of *MI-BMInet* is overall comparable to SoA works. More specifically, *MI-BMInet* sets the new SoA accuracy in both 3- and 4-class tasks of the MM/MI dataset while requiring at least one order of magnitude less memory and MACC operations compared to the previous SoA works [24], [37]. It achieves slightly worse CV accuracy (-0.47%) in the 2-class task compared to [28] at the advantage of two orders of magnitude fewer parameters, $3.2\times$ less memory for storing the feature maps, and $22.26\times$ less computation. When looking at the IV-2a dataset, our model is only 0.64% and 1.32% less accurate in the full-channel configuration for 2- and 4-class tasks compared to the SoA works [21] and [33], respectively. However, the resource requirements are orders of magnitude lower. The accuracy is further improved when the automatic channel selection is applied, as discussed in the next section.

TABLE III: Resource requirements and classification accuracy of *MI-BMInet* using all channels.

(a) Resource requirements for 4-class task.						
Layer	BCI Comp. IV-2a			Physionet MM/MI		
	#params	f. map size	#MACC	#params	f. map size	#MACC
Input		16,500			30,720	
Φ^1	704+128	24,000	528,000	1,024+64	7,680	491,520
Φ^2	2,048+128	3,000	1,536,000	2,048+64	960	983,040
Φ^3	1,536+128	176	96,000	512+64	112	30,720
Φ^4	1,412	4	704	484	4	448
Tot.	6,084	43,680	2,209,408	4,228	39,476	1,505,728

(b) Accuracy (%) before and after quantization.						
	BCI Comp. IV-2a			Physionet MM/MI		
	2-	3-	4-class	2-	3-	4-class
float-32	86.32	80.37	76.03	82.79	74.92	65.62
int-8	86.52	80.05	75.63	82.61	75.12	65.31

B. EEG Channel Selection

As shown in Fig. 5, our automatic method consistently outperforms the manual selection methods. It can reduce on average the number of channels down to 9, 11, and 14 across the 9 subjects of the IV-2a dataset while retaining similar average accuracy (86.21%, 79.91%, 75.84%) as the baseline, represented with solid lines (86.32%, 80.37%, 76.03%), respectively for the 2-, 3-, and 4-class tasks. In some cases, slightly better accuracy is achieved compared to the full-channel baseline thanks to the subject-specific methodology. In fact, by selecting the best number of channels for each subject, we obtain an improvement in the average accuracy of up to 1.33%, as reported in Table IV. The number of channels can be reduced down to 4, 14, and 11, respectively for 2-, 3-, and 4-class tasks while improving the accuracy by up to 2.95% (S1), 1.84% (S1), and 1.81% (S6) compared to the full-channel configuration. The best performing subjects for 2-, 3-, and 4-class tasks are respectively S8, S3, and S3, reaching up to 98.27%, 92.18%, and 90.97% with 6, 18, and 18 electrodes.

TABLE IV: Classification accuracy (%) / kappa score with all channels and the best accuracy / kappa score for each subject with the corresponding number of selected channels (in brackets) of BCI Competition IV-2a dataset and comparison with related works. The subjects with the best accuracy and the lowest number of selected channels and the best average accuracy over the nine subjects are highlighted in bold.

S.	2-class				3-class		4-class			
	<i>MI-BMInet</i>		CSP and E-CSP [26]		<i>MI-BMInet</i>		<i>MI-BMInet</i>		CSP+Riem. [34]	
	all ch.	sel. ch.	all ch.	sel. ch.	all ch.	sel. ch.	all ch.	sel. ch.	sel. ch.	
1	84.03/0.68	86.98/0.74 (4)	90.78/-	83.36/-(9)	89.43/0.84	91.18/0.87 (14)	83.10/0.78	84.41/0.80 (20)	87.51/0.81 (14)	
2	71.15/0.42	72.65/0.45 (20)	59.85/-	71.83/-(11)	65.74/0.49	68.76/0.53 (16)	59.27/0.46	60.49/0.47 (18)	58.32/0.44 (18)	
3	94.95/0.90	94.95/0.90 (22)	97.81/-	98.54/-(13)	91.67/0.88	92.18/0.88 (18)	90.64/0.88	90.97/0.88 (18)	89.01/0.86 (14)	
4	74.38/0.49	76.66/0.53 (9)	68.10/-	74.13/-(3)	75.66/0.64	76.00/0.64 (14)	69.77/0.60	70.63/0.61 (18)	71.12/0.63 (15)	
5	92.00/0.84	93.84/0.88 (4)	68.88/-	71.11/-(4)	79.17/0.70	80.33/0.71 (18)	71.83/0.62	73.61/0.65 (19)	63.44/0.49 (19)	
6	79.48/0.59	81.11/0.62 (20)	66.67/-	73.14/-(8)	63.48/0.45	65.56/0.49 (20)	58.10/0.44	59.91/0.47 (11)	60.16/0.53 (11)	
7	90.51/0.81	91.17/0.82 (20)	82.14/-	83.57/-(6)	88.49/0.83	88.97/0.84 (18)	84.71/0.80	85.76/0.81 (19)	93.14/0.92 (15)	
8	98.06/0.96	98.27/0.97 (6)	97.01/-	96.26/-(14)	88.18/0.82	88.63/0.83 (19)	84.55/0.80	86.48/0.82 (18)	90.43/0.86 (17)	
9	92.31/0.85	93.26/0.87 (14)	93.84/-	94.61/-(5)	81.53/0.72	82.05/0.73 (20)	82.33/0.76	82.36/0.77 (18)	87.21/0.83 (14)	
Avg.	86.32/0.74	87.65/0.75 (13.22)	80.56/-	83.61/-(8.11)	80.37/0.71	81.52/0.72 (17.44)	76.03/0.68	77.18/0.70 (17.67)	77.82/0.71 (15.2)	
Std.	8.96/0.18	8.42/0.17 (7.11)	14.85/-	11.35/-(3.95)	9.78/0.15	9.21/0.14 (2.17)	11.11/0.15	10.86/0.15 (2.45)	13.52/0.17 (2.30)	

Our subject-specific models achieve 4.04% better accuracy than [26] for the 2-class task and 0.64% less accuracy than [34] for the 4-class task. Compared to the SoA with full-channel configuration reported in Table I, we achieve the new SoA accuracy of 87.65% and a kappa value of 0.75 for the 2-class

task.

TABLE V: Classification accuracy (%), number of parameters, maximum feature map size, and computational complexity of *MI-BMInet* and its comparison with related works on the Physionet MM/MI dataset. The estimated computational resources are calculated for the 4-class task when available, otherwise for the 2-class task. The best solution for each configuration and metric is marked in bold.

	# ch	Tot. # params	Max. f. map size	Tot. # MACC	Accuracy		
					2-	3-	4-class
S.ConvNet [37]	64	203 k	1,260 k	86.12 M	80.38	69.82	58.58
CNN [28]	64	235 k	122.88 k	33.61 M	83.26	-	-
EEGNet [23]*	64	3.17 k	277.56 k	48.17 M	82.29 [‡]	74.46 [‡]	64.85 [‡]
<i>MI-BMInet</i>	64	4.23 k	38.40 k	1.51 M	82.79	74.92	65.62
EEGNet [23]*	38	2.76 k	164.16 k	24.81 M	81.86	74.12	64.65
<i>MI-BMInet</i>	38	3.81 k	25.92 k	1.31 M	82.76	74.93	64.91
CNN [28]	32	232 k	61.44 k	15.82 M	82.90	-	-
<i>MI-BMInet</i>	32	3.49 k	24.11 k	1.26 M	82.82	74.42	64.38
EEGNet [23]*	19	2.35 k	82.08 k	11.02 M	81.95	72.41	62.55
<i>MI-BMInet</i>	19	3.51 k	16.8 k	1.16 M	82.78	74.02	63.69
S.ConvNet [37]	16	126 k	314.88 k	21.6 M	78.03	-	-
<i>MI-BMInet</i>	16	3.23 k	15.36 k	1.14 M	82.63	73.47	63.47
S.ConvNet [37]	14	123 k	275.52 k	18.92 M	76.66	-	-
CNN [28]	14	231 k	26.88 k	6.68 M	82.34	-	-
<i>MI-BMInet</i>	14	3.20 k	14.40 k	1.12 M	82.64	72.89	63.30
<i>MI-BMInet</i>	10	3.14 k	12.48 k	1.09 M	82.51	71.55	61.94
S.ConvNet [37]	9	115 k	177.12 k	12.20 M	75.85	-	-
<i>MI-BMInet</i>	9	3.12 k	12.00 k	1.08 M	82.06	71.24	61.44
EEGNet [23]*	8	2.28 k	34.56 k	4.30 M	78.07	68.99	58.55
<i>MI-BMInet</i>	8	3.33 k	11.52 k	1.08 M	81.60	70.28	60.71
S.ConvNet [37]	3	106 k	59.04 k	4.13 M	73.20	-	-
<i>MI-BMInet</i>	3	3.03 k	9.12 k	1.04 M	77.42	61.66	50.12

* Adapted and deployed by [24].

‡ Reproduced. Average accuracy over 5 repetitions.

The results on the MM/MI dataset demonstrate once again that the automatic method outperforms the manual methods, except for 3- and 4-class tasks when less than 4 channels are selected, while for the 2-class task it always achieves better accuracy. In general, the simpler the task (i.e., 2-class), the less drop in accuracy from the baseline. More specifically, we achieve almost the same accuracy as the baseline (82.79% and 74.92%) down to 10 and 20 channels (82.51% and 74.21%) using the proposed automated method for the 2- and 3-class classification, afterwards the accuracy starts to drop. For the 4-class task, the accuracy drop is more significant, i.e., -1.69%, when reducing the number of channels to 18.

Table V reports the comparison with the related works. Tokovarov et al. [28] use correlation maps from output feature maps of spatial convolution layer to select relevant EEG channels. While their full model achieves 0.47% better accuracy than ours, at the cost of two orders of magnitude more memory requirement and $22\times$ more complexity, our channel selection method yields less accuracy drop (-0.15%) than theirs (-0.92%) using 14 EEG channels. The authors did not further reduce the number of channels. Compared to [37], [24], our method always achieves better accuracy at lower resource requirements. More specifically, in 14-channel configuration, it achieves 5.98% better accuracy with $38.5\times$ fewer parameters, $19.1\times$ smaller feature map size, and $16.9\times$ less computation than [37]. With our method based on spatial filters, we can decrease the number of EEG channels down to 10, i.e., by a factor of $6.4\times$, and still achieve better accuracy than the related works with full-channel configuration [37], [24], proving the effectiveness of our methods to extract relevant features for the underlying task. Compared to the baseline *MI-BMInet* with 64 EEG channels, using only 10 channels brings the advantage of $1.3\times$ fewer parameters, $3.1\times$ less memory requirement, and $1.4\times$ less complexity in terms of MACCs, while retaining a similar classification accuracy of 82.51%.

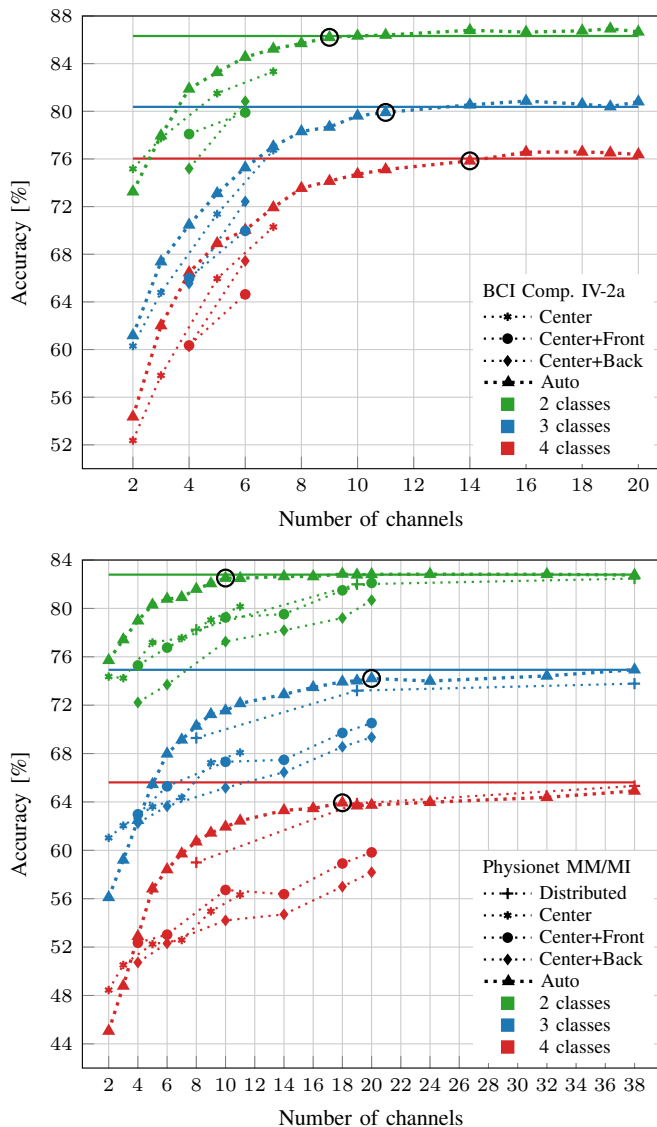


Fig. 5: Channel selection accuracy averaged over subjects for BCI Competition IV-2a dataset (top) and over CV folds for Physionet MM/MI dataset (bottom). The optimal numbers of channels are circled.

C. Embedded implementation

As reported in Table IIIb the quantized models achieve similar accuracy as the full-precision ones, with a maximum of 0.4% accuracy loss. The quantization of both weights and activations allows $4\times$ reduction of the total memory footprint. More specifically, the memory requirement is reduced from around 186 kB and 171 kB when using 32-bit representation down to roughly 47 kB and 42 kB with 8-bit quantization, respectively for IV-2a and MM/MI datasets. Recall that the fast L1 memory of Mr. Wolf is only 64 kB [22]. This means that the data transfer between the L1 and the L2 memory during the computation of a single layer is effectively eliminated after quantization reducing potential overheads and engineering efforts. As illustrated in Fig. 6, all related works based on CNNs, except for Q-EEGNet [18], do not fit in the on-chip

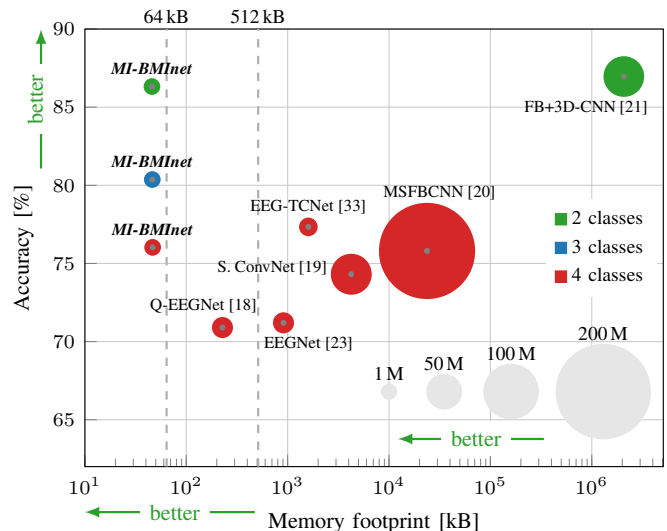


Fig. 6: Accuracy vs. memory footprint for the BCI Competition IV-2a dataset. The computational complexity in terms of MACCs is represented as the size of the circles. The vertical lines mark the L1 and L2 on-chip memory of Mr. Wolf.

fast memory of Mr. Wolf. Whereas, the memory requirement of the quantized *MI-BMNet* is up to five orders of magnitude lower, and it is within the memory availability of the L1 fast memory of the compute cluster of Mr. Wolf. It also requires the least amount of MACC operations and achieves similar accuracy as the SoA works.

Table VI reports the inference time and the power measurements of the deployed models on Mr. Wolf with both fabric controller and the cluster cores running at 50 MHz and supplied with 0.8 V. The measured runtime, including the cluster startup, is 11.4 ms on average for the IV-2a dataset in full-channel configuration and 6.21 ms on average for the MM/MI dataset. The average power consumption is respectively 10.11 mW and 9.96 mW, yielding an average energy consumption of 114.93 μ J and 61.87 μ J. The consumption is

TABLE VI: Networks deployment. The average power consumption (SoC + cluster domains) and the runtime per inference including the cluster startup time are measured at 50 MHz with 0.8 V power supply.

Dataset	BCI Comp.				Physionet			
	4	3	2	2	4	3	2	2
Num. classes	4	3	2	2	4	3	2	2
Num. channels	22	22	22	6 [†]	64	64	64	10 [‡]
(Q) Accuracy (%)	75.63	80.05	86.52	97.76	65.31	75.12	82.61	82.51
Est. Memory (kB)	46.58	46.23	45.88	33.37	42.63	42.52	42.40	15.62
Est. #MACCs (M)	2.21	2.21	2.21	1.82	1.51	1.51	1.51	1.09
Time/infer. (ms)	11.37	11.43	11.30	10.57	6.21	6.21	6.21	5.53
Avg. power (mW)	10.07	10.03	10.24	9.7	9.92	9.97	10.00	9.06
Energy/infer. (μ J)	114.5	114.6	115.7	102.5	61.60	61.91	62.10	50.10
Throughput (MMACCs/s)	194.3	193.3	195.5	172.6	242.5	242.5	242.4	197.2
En. Eff. (GMACCs/s/W)	19.30	19.27	19.09	17.80	24.44	24.32	24.24	21.77

[†] Subject 8. Selected channels: CP3, P1, POz, CP4, C6, FC4.

[‡] Fold 1. Sel. channels: AF8, F8, T8, C3, Cz, C2, CP2, CP5, F6, T9.

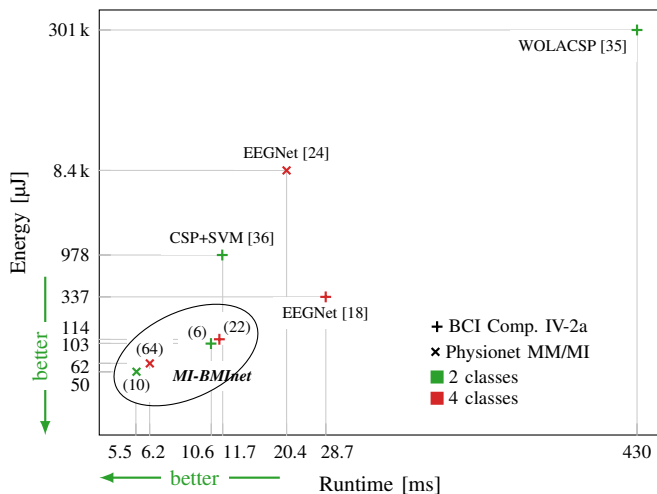


Fig. 7: Energy consumption vs. runtime. The number of EEG channels used for *MI-BMInet* is reported in brackets.

further reduced thanks to channel selection, as illustrated in Fig. 7. Considering the best performing subject 8 (S8, 98.27% accuracy) of the IV-2a dataset on 2-class task, the number of EEG channels can be reduced down to 6 while keeping similar classification accuracy (97.76%), yielding an energy reduction of 11.4% compared to the usage of all 22 channels. The same conclusion can be drawn for the subject-independent MM/MI dataset. For the 2-class task, the number of channels is reduced by a factor of 6.4 \times , i.e., from 64 down to 10, without significant accuracy loss. This translates into a runtime speedup of 1.12 \times and an energy reduction of almost 20%, i.e., 50.10 μ J. Overall, the highest achieved throughput is 242.5MMACCs/s with an energy efficiency of 24.44GMACCs/s/W. Compared to the related works, our proposed implementation is orders of magnitude faster and less energy-hungry, as shown in Fig. 7.

VIII. DISCUSSION

The proposed CNN achieves similar accuracy to the SoA while being much more hardware-friendly than related works. The proposed channel reduction algorithm further reduces the resource requirements while retaining similar or slightly higher accuracy. This means that it is an effective method to identify the most relevant electrodes for the classification task. In the subject-specific case, the accuracy is improved when the number of channels and the electrodes are selected specifically for each subject. As shown in Fig. 8, the average ℓ_2 -norm of the spatial filters of the subject-specific *MI-BMInet* models has a different distribution over the scalp for each subject. Each model learns subject-specific spatial filters. The higher values of the ℓ_2 -norm, which we call ‘activations’ for shorthand, represented with darker red color, are found near the electrodes C3, C4 over the sensorimotor cortex and from the Cz to POz over the temporal lobe. Future work can further exploit the subject-specificity and customize the hyperparameters of the *MI-BMInet* using neural architecture search, e.g., by tuning the number of spatial and temporal filters as in [33], where

the authors improve the accuracy from 77.34% to 83.84% by tuning the network architecture for each subject.

Nevertheless, training models in a subject-specific manner yields longer development time and is not transferable directly to new users. We additionally evaluate subject-independent models on the larger MM/MI dataset to find relevant EEG channels and, accordingly, the regions of the brain cortex important for solving the MI tasks across multiple subjects. This is important for the product development of a general MI EEG headset such as Melomind [48]. In Fig. 4, we see that the usage of distributed electrodes yields much better results than the headphone configurations, especially for the 3- and 4-class tasks. This suggests that regions outside the sensorimotor cortex are also relevant for classifying the ‘rest’ and ‘feet’ classes for this dataset. Fig. 9 shows the topographic maps of the average ℓ_2 -norm of the weights in the spatial filters over 5-fold CV and 5 repetitions. As previously found in the literature [49], [52], the motor cortex is activated during MM and MI. For the 2-class task, the regions under electrodes C3 and C4 are important for left- and right-hand movements [12], [52], while the addition of the ‘rest’ class in the 3-class task introduces cerebral activation captured by the electrode Iz placed on inion over the occipital lobe. Finally, the addition of the fourth class of imagining the movement of both feet yields neural activity under the electrode Cz which is confirmed in the literature [12], [53].

In all the heatmaps, we observe activations near electrodes F7 and F8, which are not present in Fig. 8 due to the lack of these electrodes in the dataset. These are found to be covering the inferior frontal gyrus [54] near the Sylvian fissure [55] between the frontal and temporal lobe, where the insular cortex is also located. This area is considered relevant in attentional elaborations and working memory processing related to external stimuli [56], [57]. Being part of the dorsal frontoparietal network, it has a top-down control function over motor and sensory areas with basic cognitive selection of sensory information and response [58]. Moreover, a study suggests that it plays a role in motor planning and imagery [59]. A similar line of research on the insular cortex, saccade system, and supplementary motor areas further confirms the involvement of this area in motor control, attentional fixation, and responses to switching stimuli [60], [61]. These pieces of evidence lead to the conclusion that the activation of this area is likely due to the presentation of the cue and the experimental protocol of the MM/MI dataset [46]. However, another study [37] suggests that the activities in this area are due to electromyographic and electrooculographic artifacts [37]. Depending on the acquisition setup, this is also a valid hypothesis since the electrodes F7 and F8 are prone to collect muscular and ocular artifacts [62]. An acquisition procedure that eliminates the dependency on the visual cue is helpful in future research to further investigate the real nature of this activation. A possible solution is to design an experimental paradigm combined with electromyograms as in [63].

A related topic is the detection of movement intention. For a real-world IoM scenario, no visual cue is presented to the subject marking the MI’s start. Hence, algorithms that

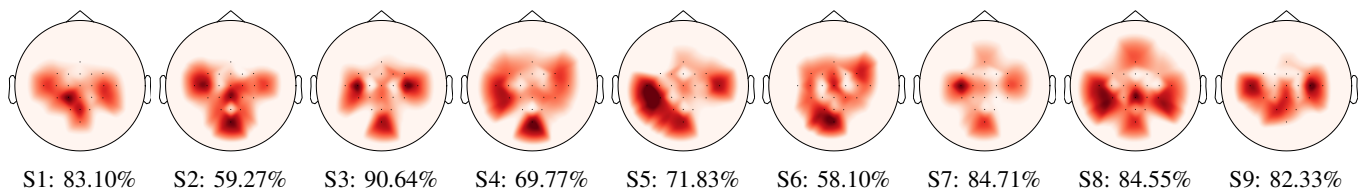


Fig. 8: Heatmaps of ℓ_2 -norm of the weights in the spatial filters for BCI Competition IV2a dataset for all 9 subjects with average accuracy over 25 repetitions in full-channel configuration. The average accuracy over all the subjects is 76.03%.

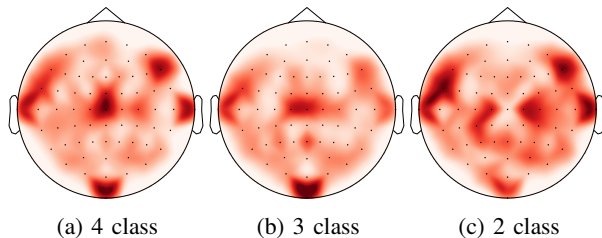


Fig. 9: Heatmaps of ℓ_2 -norm of weights in spatial filters for Physionet MM/MI dataset.

can autonomously detect the onset of the MI intention are necessary for an online BMI that is asynchronously self-paced.

IX. CONCLUSION

This paper proposes an energy-efficient embedded solution for BMI based on the MI paradigm. We propose a tiny CNN that achieves similar SoA accuracy but is orders of magnitude less resource-demanding and can operate with a variable number of EEG channels for application-specific selection. We further propose an automatic channel reduction method based on spatial filters of the proposed CNN and extract the most relevant EEG channels to effectively reduce the memory requirements, the computational complexity, and the power consumption for the embedded BMI. We finally deploy the proposed models on a PULP MCU by exploiting its hardware extensions and experimentally measure the runtime and power consumption. The final solution consumes down to 50.10 μ J and takes only 5.53 ms per inference with an accuracy of 82.51% on the 2-class MI task using only 10 out of 64 EEG channels. We successfully satisfy the three-way trade-off among accuracy, resource cost, and power usage and set the new SoA for embedded MI-BMIs.

REFERENCES

- [1] M. Xiong, R. Hotter, D. Nadin, J. Patel, S. Tartakovsky, Y. Wang, H. Patel, C. Axon, H. Bosiljevac, A. Brandenberger *et al.*, "A low-cost, semi-autonomous wheelchair controlled by motor imagery and jaw muscle activation," in *Proc. IEEE International Conference on Systems, Man and Cybernetics (SMC)*, 2019, pp. 2180–2185.
- [2] M. Vilela and L. R. Hochberg, "Chapter 8 - applications of brain-computer interfaces to the control of robotic and prosthetic arms," in *Brain-Computer Interfaces*, ser. Handbook of Clinical Neurology, N. F. Ramsey and J. del R. Millán, Eds. Elsevier, 2020, vol. 168, pp. 87–99.
- [3] U. Chaudhary, N. Birbaumer, and A. Ramos-Murguialday, "Brain-computer interfaces for communication and rehabilitation," *Nature Reviews Neurology*, vol. 12, pp. 513–525, 08 2016.
- [4] K. K. Ang and C. Guan, "Eeg-based strategies to detect motor imagery for control and rehabilitation," *IEEE Transactions on Neural Systems and Rehabilitation Engineering*, vol. 25, no. 4, pp. 392–401, 2017.
- [5] X. Huang, E. Yin, Y. Wang, R. Saab, and X. Gao, "A mobile eeg system for practical applications," in *Proc. IEEE Global Conference on Signal and Information Processing (GlobalSIP)*, 2017, pp. 995–999.
- [6] P. Aricò, N. Sciaraffa, and F. Babiloni, "Brain-computer interfaces: Toward a daily life employment," *Brain Sciences*, vol. 10, no. 3, 03 2020.
- [7] L. Shao, L. Zhang, A. N. Belkacem, Y. Zhang, X. Chen, J. Li, and H. Liu, "Eeg-controlled wall-crawling cleaning robot using ssvep-based brain-computer interface," *Journal of Healthcare Engineering*, vol. 2020, pp. 1–11, 01 2020.
- [8] X. Zhang, L. Yao, S. Zhang, S. Kanhere, M. Sheng, and Y. Liu, "Internet of things meets brain-computer interface: A unified deep learning framework for enabling human-thing cognitive interactivity," *IEEE Internet of Things Journal*, vol. 6, no. 2, pp. 2084–2092, 2019.
- [9] N. Kobayashi and K. Ishizuka, "Lstm-based classification of multiflicker-ssvep in single channel dry-eeg for low-power/high-accuracy quadcopter-bmi system," in *Proc. IEEE International Conference on Systems, Man and Cybernetics (SMC)*, 2019, pp. 2160–2165.
- [10] A. N. Belkacem, N. Jamil, J. A. Palmer, S. Ouhbi, and C. Chen, "Brain computer interfaces for improving the quality of life of older adults and elderly patients," *Frontiers in Neuroscience*, vol. 14, p. 692, 2020.
- [11] D. Freer and G.-Z. Yang, "Data augmentation for self-paced motor imagery classification with c-lstm," *Journal of Neural Engineering*, vol. 17, no. 1, p. 016041, 01 2020.
- [12] G. Pfurtscheller and F. Lopes da Silva, "Event-related EEG/MEG synchronization and desynchronization: basic principles," *Clinical Neurophysiology*, vol. 110, no. 11, pp. 1842–1857, 11 1999.
- [13] J. Zhuang, K. Geng, and G. Yin, "Ensemble learning based brain-computer interface system for ground vehicle control," *IEEE Transactions on Systems, Man, and Cybernetics: Systems*, vol. 51, no. 9, pp. 5392–5404, 2021.
- [14] E. Tunstel, M. J. Cobo, E. Herrera-Viedma, I. J. Rudas, D. Filev, L. Trajkovic, C. L. P. Chen, W. Pedrycz, M. H. Smith, and R. Kozma, "Systems science and engineering research in the context of systems, man, and cybernetics: Reflection, trends, and future directions," *IEEE Transactions on Systems, Man, and Cybernetics: Systems*, vol. 51, no. 1, pp. 5–21, 2021.
- [15] A. Casson, "Wearable eeg and beyond," *Biomedical Engineering Letters*, vol. 9, pp. 53–71, 01 2019.
- [16] C. Beach, E. Balaban, and A. J. Casson, "Chapter 14 - edge algorithms for wearables: an overview of a truly multi-disciplinary problem," in *Wearable Sensors*, 2nd ed., E. Sazonov, Ed. Oxford: Academic Press, 2021, pp. 379–414.
- [17] V. Kartsch, G. Tagliavini, M. Guermandi, S. Benatti, D. Rossi, and L. Benini, "Biowolf: A sub-10-mw 8-channel advanced brain-computer interface platform with a nine-core processor and ble connectivity," *IEEE Transactions on Biomedical Circuits and Systems*, vol. 13, no. 5, pp. 893–906, 2019.
- [18] T. Schneider, X. Wang, M. Hersche, L. Cavigelli, and L. Benini, "Q-eegnet: an energy-efficient 8-bit quantized parallel eegnet implementation for edge motor-imagery brain-machine interfaces," in *Proc. IEEE International Conference on Smart Computing (SMARTCOMP)*, 2020, pp. 284–289.
- [19] R. T. Schirmer, J. T. Springenberg, L. D. J. Fiederer, M. Glasstetter, K. Eggenberger, M. Tangermann, F. Hutter, W. Burgard, and T. Ball, "Deep learning with convolutional neural networks for EEG decoding and visualization," *Human Brain Mapping*, vol. 38, no. 11, pp. 5391–5420, 2017.
- [20] H. Wu, Y. Niu, F. Li, Y. Li, B. Fu, G. Shi, and M. Dong, "A Par-

- allel Multiscale Filter Bank Convolutional Neural Networks for Motor Imagery EEG Classification,” *Frontiers in Neuroscience*, vol. 13, 11.
- [21] J. S. Bang, M. H. Lee, S. Fazli, C. Guan, and S. W. Lee, “Spatio-spectral feature representation for motor imagery classification using convolutional neural networks,” *IEEE Transactions on Neural Networks and Learning Systems*, pp. 1–12, 2021.
- [22] A. Pullini, D. Rossi, I. Loi, G. Tagliavini, and L. Benini, “Mr.Wolf: An Energy-Precision Scalable Parallel Ultra Low Power SoC for IoT Edge Processing,” *IEEE Journal of Solid-State Circuits*, vol. 54, no. 7, pp. 1970–1981, 2019.
- [23] V. J. Lawhern, A. J. Solon, N. R. Waytowich, S. M. Gordon, C. P. Hung, and B. J. Lance, “EEGNet: a compact convolutional neural network for EEG-based brain–computer interfaces,” *Journal of Neural Engineering*, vol. 15, no. 5, p. 056013, 2018.
- [24] X. Wang, M. Hersche, B. Tömecke, B. Kaya, M. Magno, and L. Benini, “An accurate eegnet-based motor-imagery brain–computer interface for low-power edge computing,” in *2020 IEEE International Symposium on Medical Measurements and Applications (MeMeA)*, 2020, pp. 1–6.
- [25] Y. Li, Y. Chen, X. Dai, D. Chen, M. Liu, L. Yuan, Z. Liu, L. Zhang, and N. Vasconcelos, “Micronet: Towards image recognition with extremely low flops,” *ArXiv*, vol. abs/2011.12289, 2020.
- [26] A. K. Das and S. Suresh, “An effect-size based channel selection algorithm for mental task classification in brain computer interface,” in *2015 IEEE International Conference on Systems, Man, and Cybernetics*, 2015, pp. 3140–3145.
- [27] B. Chen, Y. Li, J. Dong, N. Lu, and J. Qin, “Common spatial patterns based on the quantized minimum error entropy criterion,” *IEEE Transactions on Systems, Man, and Cybernetics: Systems*, vol. 50, no. 11, pp. 4557–4568, 2020.
- [28] M. Tokovarov, “Convolutional neural networks with reusable full-dimension-long layers for feature selection and classification of motor imagery in eeg signals,” in *Artificial Neural Networks and Machine Learning – ICANN 2020*, I. Farkas, P. Masulli, and S. Wermter, Eds. Cham: Springer International Publishing, 2020, pp. 79–91.
- [29] M. Spallanzani, L. Cavigelli, G. Leonardi, M. Bertogna, and L. Benini, “Additive noise annealing and approximation properties of quantized neural networks,” *arXiv:1905.10452*, 05 2019.
- [30] L. Cavigelli and L. Benini, “RPR: Random Partition Relaxation for Training; Binary and Ternary Weight Neural Networks,” *arXiv:2001.01091*, 2020.
- [31] R. Das, P. S. Lopez, M. Ahmed Khan, H. K. Iversen, and S. Puthusserypady, “Fbcsp and adaptive boosting for multiclass motor imagery bci data classification: A machine learning approach,” in *Proc. IEEE International Conference on Systems, Man, and Cybernetics (SMC)*, 2020, pp. 1275–1279.
- [32] M. Hersche, T. Rellstab, P. D. Schiavone, L. Cavigelli, L. Benini, and A. Rahimi, “Fast and Accurate Multiclass Inference for MI-BCIs Using Large Multiscale Temporal and Spectral Features,” in *Proc. 26th European Signal Processing Conference (EUSIPCO)*. IEEE, 9 2018, pp. 1690–1694.
- [33] T. M. Ingolfsson, M. Hersche, X. Wang, N. Kobayashi, L. Cavigelli, and L. Benini, “Eeg-tcnet: An accurate temporal convolutional network for embedded motor-imagery brain–machine interfaces,” in *Proc. IEEE International Conference on Systems, Man, and Cybernetics (SMC)*, 2020, pp. 2958–2965.
- [34] S. Chen, Y. Sun, H. Wang, and Z. Pang, “Channel selection based similarity measurement for motor imagery classification,” in *Proc. IEEE International Conference on Bioinformatics and Biomedicine (BIBM)*, 2020, pp. 542–548.
- [35] K. Belwafi, O. Romain, S. Gannouni, F. Ghaffari, R. Djemal, and B. Ouni, “An embedded implementation based on adaptive filter bank for brain–computer interface systems,” *Journal of Neuroscience Methods*, vol. 305, pp. 1–16, 2018.
- [36] A. Malekmohammadi, H. Mohammadzade, A. Chamanzar, M. Shabany, and B. Hjojogh, “An efficient hardware implementation for a motor imagery brain computer interface system,” *Scientia Iranica*, vol. 26, no. Special Issue on: Socio-Cognitive Engineering, pp. 72–94, 2019.
- [37] H. Dose, J. S. Möller, H. K. Iversen, and S. Puthusserypady, “An end-to-end deep learning approach to mi-eeg signal classification for bcis,” *Expert Systems with Applications*, vol. 114, pp. 532–542, 2018.
- [38] H. Ramoser, J. Muller-Gerking, and G. Pfurtscheller, “Optimal spatial filtering of single trial eeg during imagined hand movement,” *IEEE Transactions on Rehabilitation Engineering*, vol. 8, no. 4, pp. 441–446, 2000.
- [39] K. K. Ang, Z. Y. Chin, C. Wang, C. Guan, and H. Zhang, “Filter bank common spatial pattern algorithm on bci competition iv datasets 2a and 2b,” *Frontiers in Neuroscience*, vol. 6, p. 39, 2012.
- [40] F. Yger, M. Berar, and F. Lotte, “Riemannian Approaches in Brain-Computer Interfaces: A Review,” *IEEE Transactions on Neural Systems and Rehabilitation Engineering*, vol. 25, no. 10, pp. 1753–1762, 10 2017.
- [41] A. L. Goldberger, L. A. N. Amaral, L. Glass, J. M. Hausdorff, P. C. Ivanov, R. G. Mark, J. E. Mietus, G. B. Moody, C.-K. Peng, and H. E. Stanley, “PhysioBank, PhysioToolkit, and PhysioNet: components of a new research resource for complex physiologic signals,” *circulation*, vol. 101, no. 23, pp. e215–e220, 2000.
- [42] R. David, J. Duke, A. Jain, V. J. Reddi, N. Jeffries, J. Li, N. Kreeger, I. Nappier, M. Natraj, S. Regev, R. Rhodes, T. Wang, and P. Warden, “Tensorflow lite micro: Embedded machine learning on tinyml systems,” *arXiv:2010.08678*, 2021.
- [43] T. Foundation, “tinyml®,” <https://www.tinyml.org/>, 2021, accessed: 2021-05-27.
- [44] C. Brunner, R. Leeb, G. R. Müller-Putz, A. Schlögl, and G. Pfurtscheller, “BCI competition 2008 - Graz data set A,” doi: 10.1007/BF00994018.
- [45] M. Tangermann, K.-R. Müller, A. Aertsen, N. Birbaumer, C. Braun, I. Brunner, R. Leeb, C. Mehring, K. Müller, G. Mueller-Putz, G. Nolte, G. Pfurtscheller, H. Preissl, G. Schalk, A. Schlögl, C. Vidaurre, S. Waldert, and B. Blankertz, “Review of the bci competition iv,” *Frontiers in Neuroscience*, vol. 6, p. 55, 2012.
- [46] G. Schalk, D. McFarland, T. Hinterberger, N. Birbaumer, and J. Wolpaw, “BCI2000: A General-Purpose Brain-Computer Interface (BCI) System,” *IEEE Transactions on Biomedical Engineering*, vol. 51, no. 6, pp. 1034–1043, 6 2004.
- [47] N. M. LLC, “Versus: a mobile eeg headset,” <https://getversus.com/>, 2021, accessed: 2021-10-11.
- [48] G. Spinelli, A. Odouard, M.-C. Nierat, S. Champion, M. Bensoussan, F. Grosselin, K. Pandremmenou, A. Breton, M. Raux, Y. Atal, T. Similowski, and X. Navarro-Suné, “Validation of melomind™ signal quality: a proof of concept resting-state and erps study,” *bioRxiv:2020.02.28.969808*, 2020.
- [49] G. Pfurtscheller and C. Neuper, “Motor imagery activates primary sensorimotor area in humans,” *Neuroscience Letters*, vol. 239, no. 2, pp. 65 – 68, 1997.
- [50] B. Jacob, S. Kligys, B. Chen, M. Zhu, M. Tang, A. Howard, H. Adam, and D. Kalenichenko, “Quantization and training of neural networks for efficient integer-arithmetic-only inference,” in *Proc. IEEE CVPR*, 2018, pp. 2704–2713.
- [51] X. Wang, “DSP library for PULP,” <https://github.com/pulp-platform/pulp-dsp>, 2019.
- [52] C. Neuper, M. Wörtz, and G. Pfurtscheller, “Erd/ers patterns reflecting sensorimotor activation and deactivation,” in *Event-Related Dynamics of Brain Oscillations*, ser. Progress in Brain Research, C. Neuper and W. Klimesch, Eds. Elsevier, 2006, vol. 159, pp. 211–222.
- [53] M. Zhao, M. Marino, J. Samogin, S. P. Swinnen, and D. Mantini, “Hand, foot and lip representations in primary sensorimotor cortex: a high-density electroencephalography study,” *Brain Connectivity*, vol. 9, pp. 2045–2322, 2019.
- [54] R. Homan, J. Herman, and P. Purdy, “Cerebral location of international 10-20 system electrode placement,” *Electroencephalography and Clinical Neurophysiology*, vol. 66, no. 4, pp. 376–82, 1987.
- [55] V. L. Towle, J. Bolaños, D. Suarez, K. Tan, R. Grzeszczuk, D. N. Levin, R. Cakmur, S. A. Frank, and J.-P. Spire, “The spatial location of eeg electrodes: locating the best-fitting sphere relative to cortical anatomy,” *Electroencephalography and Clinical Neurophysiology*, vol. 86, no. 1, pp. 1–6, 1993.
- [56] M. Tops and M. Boksem, “A potential role of the inferior frontal gyrus and anterior insula in cognitive control, brain rhythms, and event-related potentials,” *Frontiers in Psychology*, vol. 2, p. 330, 2011.
- [57] M. Corbetta, G. Patel, and G. Shulman, “The reorienting system of the human brain: from environment to theory of mind,” *Neuron*, vol. 58, no. 3, pp. 306–24, 2008.
- [58] M. Corbetta and G. Shulman, “Control of goal-directed and stimulus-driven attention in the brain,” *Nature Reviews Neuroscience*, vol. 3, no. 3, pp. 201–15, 2008.
- [59] R. Ptak, A. Schnider, and J. Fellrath, “The dorsal frontoparietal network: A core system for emulated action,” *Trends in Cognitive Sciences*, vol. 21, no. 8, pp. 589–599, 2017.
- [60] T. J. Anderson, I. H. Jenkins, D. J. Brooks, M. B. Hawken, R. S. J. Frackowiak, and C. Kennard, “Cortical control of saccades and fixation in man A PET study,” *Brain*, vol. 117, no. 5, pp. 1073–1084, 10 1994.
- [61] P. Nachev, C. Kennard, and M. Husain, “Functional role of the supplementary and pre-supplementary motor areas,” *Nature Reviews Neuroscience*, vol. 9, no. 11, pp. 856–869, 2008.

- [62] M. Sazgar and M. G. Young, *EEG Artifacts*. Cham: Springer International Publishing, 2019, pp. 149–162.
- [63] R. Xu, N. Jiang, N. Mrachacz-Kersting, C. Lin, G. Asín Prieto, J. C. Moreno, J. L. Pons, K. Dremstrup, and D. Farina, “A closed-loop brain–computer interface triggering an active ankle–foot orthosis for inducing cortical neural plasticity,” *IEEE Transactions on Biomedical Engineering*, vol. 61, no. 7, pp. 2092–2101, 2014.